

# TriphiBot: A Triphibious Robot Combining FOC-based Propulsion with Eccentric Design

Xiangyu Li, Mingwei Lai, Mengke Zhang, Junxiao Lin, Tiancheng Lai, Junping Zhi, Chao Xu, Fei Gao and Yanjun Cao

**Abstract**—Triphibious robots capable of multi-domain motion and cross-domain transitions are promising to handle complex tasks across diverse environments. However, existing designs primarily focus on dual-mode platforms, and some designs suffer from high mechanical complexity or low propulsion efficiency, which limits their application. In this paper, we propose a novel triphibious robot capable of aerial, terrestrial, and aquatic motion, by a design combining a quadcopter with two passive wheels, without extra actuators. To address inefficiency of ground-support motion (moving on land/seabed) for quadcopter based designs, we introduce an eccentric Center of Gravity (CoG) design that inherently aligns thrust with motion, enhancing efficiency without mechanical designs. Furthermore, to address the differences in motion control caused by different fluids (air and water), we develop a unified propulsion system based on Field-Oriented Control (FOC). This method resolves torque matching issues and enables precise, rapid bidirectional thrust across different mediums. Grounded in the perspective of living condition and ground support, we analyse the robot's dynamics and propose a Hybrid Nonlinear Model Predictive Control (HNMPc)-PID control system to ensure stable multi-domain motion and seamless transitions. Experimental results validate the robot's multi-domain motion and cross-mode transition capability, along with the efficiency and adaptability of the propulsion system.

**Index Terms**—Triphibious robot, eccentric design, multi-domain motion, field-oriented control, torque matching.

## I. INTRODUCTION

CROSS-DOMAIN mobility has attracted enormous attention due to the potential to tackle complex tasks across various environments [1], [2]. Aerial mobility provides rapid response speed and a bird's-eye view in three-dimensional space; ground mobility has efficient energy consumption, and a viewpoint from ground; and swimming capability enables underwater inspection, thus enhancing survivability in most working environments. A single robot that can freely move in different conditions and provides seamless transitions between different mediums is highly desirable for missions in hazardous or complex areas, such as search and rescue and the exploration of unknown environments. However, current research remains predominantly confined to dual-mode robots, such as

This work was supported by China National Tobacco Corporation under Grant 110202402018. (Corresponding author: Yanjun Cao, Junping Zhi.)

Xiangyu Li, Mingwei Lai, Mengke Zhang, Junxiao Lin, Tiancheng Lai, Chao Xu, Fei Gao and Yanjun Cao are with the State Key Laboratory of Industrial Control Technology, Zhejiang University, Hangzhou 310027, China, and also with the Huzhou Institute of Zhejiang University, Huzhou 313000, China (email: xiangyu.li@zju.edu.cn; yanjunhi@zju.edu.cn)

Junping Zhi is with Hainan Red Tower Cigarette Co., Ltd., Hainan 571100, China.



Fig. 1. A depiction of the mission profile of TriphiBot, a triphibious robot that has the capability of flying in the air, swimming in water, and moving on land or the seabed, with smooth cross-domain, cross-mode transitions.

land-air or water-air platforms [3], [4]. While demonstrating considerable progress, these systems are inherently limited to two operational domains. A few results about triphibious robots adopt a design of a quadcopter and passive wheels, which gently demonstrate their application in three different environments [5], [6], [7]. However, they still lack the ability for seamless cross-domain movement.

The prevailing approach in cross-domain robots when involving flying is to use a multi-rotor drone as the base platform. These systems achieve motion in the air through the thrust generated by their rotors [3], [8]. To achieve ground motion, [9], [10] rely on active wheels, which severely compromise flight efficiency due to their added drive system weight. Consequently, the passive-wheeled approach, which utilizes the horizontal component of rotor thrust to drive the robot's horizontal movement, has gained prominence due to its simple structure without many additional mechanisms [11], [12]. However, as only a small fraction of total thrust (horizontal component) is used to drive horizontal motion and the rest is still wasted to support the robot's weight, these passive-wheeled robots are less efficient on the ground [13]. To address this issue, Lai et al. [14] propose a passive wheeled scheme with a dynamically adjustable thrust direction through transformable mechanisms, combined with bidirectional rotor control, to obtain horizontal thrust aligned with the velocity, reducing the power consumption of ground mode. However, this improvement still introduces additional linkages and servo mechanisms, which not only increases the system's complexity and weight but also require additional time to complete the transition. Robot design for water-air cross-domain motion has

much less results than research on air-land robots, typically by adding a vector thrust mechanism to enhance their maneuverability in water [15], [8]. However, these designs lack the capability to operate on the seabed or on land, focusing on the driving propulsion system challenges in the air and water.

One of the key challenges in designing cross-domain amphibious robots comes from the different physical characteristics present in different environments, such as airflow or water flow. Water is more than 700 times denser than air, and its viscosity is more than 50 times greater than that of air. Considering the thrust generated by the propellers, the rotation of underwater rotors requires significantly higher torque than in air, but at a much lower rotational speed. Some solutions employ either a compromised propulsion strategy that is suitable for air alone [16], [17] or two separate propulsion units specifically designed for air and water [18], [19]. Another category involves additional mechanisms with the same actuators to solve different torque requirements, such as integrating gearbox [15], [20] or utilizing deformable propellers [4], [21]. These methods have the problem of increasing additional weight, partial underutilization of propulsion systems, and complex structure, which leads to an increase in energy consumption. The cross-domain characteristics also place different demands on the control system. In the air, with the large speed range of the rotation, thrust is typically achieved through open-loop or PID closed-loop control based on the electronic speed controller (ESC) [11], [14]. However, due to inaccuracies in ESC speed estimation, both methods face challenges in having rapid and precise control. Especially at low-speed control, the speed feedback from the ESC is with large noise, leading to delays and making it difficult to switch between positive and negative thrust quickly. This control issue becomes even more severe in aquatic environments due to the high density and viscosity of water [15], [20]. Therefore, developing a lightweight, unified propulsion system capable of accurately controlling the torque output in various environments is of great importance to designing a cross-domain amphibious robot.

Different from the previous work that simply considers the environment to define amphibious robots, we have found two main fundamental principles that need to be considered by analyzing the inherent requirements and motion of triphibious robots in depth. One is the cross-domain capability from the living condition perspective (air or water), and the other is ground support from the motion feature (flying/swimming or moving on land/seabed). Challenges come from multiple contradictory requirements and changing dynamics in different modes. Flying mode in the air asks for light weight design with minimal additional mechanical structure to have a long battery life. Underwater mode places distinct propulsion requirements, either from an extra actuator system or a specially designed mechanism to improve the thrust output. Motion on the ground results in changing dynamics by involving ground support force and friction, both on land and seabed. This necessitates a control system capable of rapidly adapting to varying environments and seamlessly switching strategies, ensuring stable posture, precise trajectory tracking, and smooth cross-domain mobility.

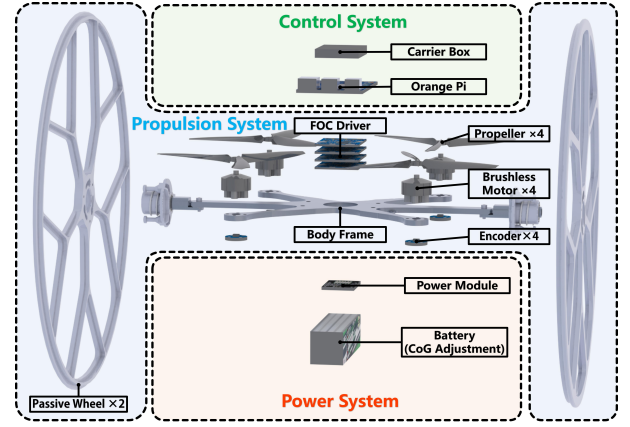


Fig. 2. Illustration of the TriphiBot's hardware layout. It can be divided into the control system, propulsion system and power system.

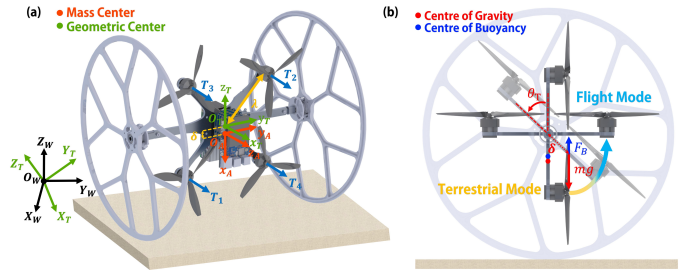


Fig. 3. (a) The coordinate frames of the dynamics model of TriphiBot. (b) Attitude transition of TriphiBot (side view).

In this article, we propose a novel design of a triphibious cross-domain robot that is physically based solely on a quadcopter structure and two passive wheels, without introducing any extra actuators or mechanisms. By shifting the center of gravity (CoG) and coupled with supporting point design, we achieve efficient ground motion without any additional structures, therefore does not introduce any extra load in air mode. Additionally, a novel unified cross-domain propulsion system based on field-oriented control (FOC) has been designed and implemented to solve the torque requirement in different mediums. The comprehensive motion strategy of the robot is depicted in Fig. 1. The contributions are summarized as follows:

- 1) We design and implement a novel triphibious robot that has the capability of flying in the air, swimming in water, and moving on land or the seabed, with smooth cross-domain, cross-mode transitions.
- 2) We propose an eccentric design with a specially chosen CoG, making the thrust direction aligned with the ground motion by default, achieving efficient ground motion without introducing any extra actuators or mechanisms.
- 3) We propose a propulsion system that integrates a field-oriented control method for cross-domain applications. This system can resolve torque matching issues and achieve fast and precise bidirectional thrust control in various mediums.
- 4) We analyze the dynamic model and differential flat-

ness of the robot in different modes, and propose a cross-domain control framework with Hybrid Nonlinear Model Predictive Control and PID control.

The rest of this article is organized as follows. Section II elaborates on the hardware design of TriphiBot. Section III establishes the dynamic models. Section IV describes the control architecture of the propulsion system and the cross-domain controller of the TriphiBot. Section V validates the motion within multiple fields and the transition ability between fields through experiments. Section VI summarizes the article.

## II. HARDWARE DESIGN

TriphiBot does not have many interesting features from the outlook; however, the design principle is novel by combining an eccentric design with a special propulsion system. TriphiBot achieves an efficient triphibious motion with a straightforward but useful solution, without any additional complex mechanisms or extra actuators involved.

### A. Structure Overview

As shown in Fig. 2, the robot is composed of a control system, a propulsion system and a power system. It can be divided into a quadcopter and two passive wheels. Fig. 3(a) defines three coordinate systems, including the world frame ( $\mathcal{F}_W$ ) where the  $z_W$  axis points in the opposite direction of the gravity vector, the geometric center frame ( $\mathcal{F}_T$ ) where  $x_T$  is perpendicular to the frame plate and  $y_T$  is aligned with the wheel axis, and the mass frame ( $\mathcal{F}_A$ ) where  $z_A$  is parallel to  $x_T$  and  $y_A$  is parallel to the wheel axis. Among them,  $O_T$  is located at the geometric center,  $O_A$  is located at the CoG, and  $O_A$  shifts a distance of  $\delta$  in the opposite direction of  $z_T$  relative to  $O_T$ .

The main novelty of TriphiBot is from the principle by leveraging the gravity and combined with special propulsion system. We specially design the position of CoG by applying the principle of the roly-poly toy. The CoG is located on the propeller plane with a small shift distance towards the front of the robot. This design make the main part of the drone, includes the propeller plane, become vertical to the ground when the wheels touch the supporting surface, either from land or seabed. When flying through the air or swimming in water, the small shift between the CoG and the centroid does not have much influence from the work. Fig. 3(b) is the side view of robot attitude transition. By leveraging gravity, the robot's thrust vector is aligned with the ground motion by default, enabling 100% of the thrust to be used for propulsion. Existing research has confirmed that robots using this method for ground movement can achieve energy savings of up to 95.37% compared to aerial flight [14]. Meanwhile, the restoring torque  $\tau_r = mg\delta \sin \theta_T$  generated by gravity provides efficient passive pitch stabilization on land or seabed. When the robot takes off from the land and seabed, it controls the pitch angle until its thrust is perpendicular to the horizontal plane.

TriphiBot has two passive wheels installed on two sides of the body and four motors are symmetrically arranged around the frame. The upper section of the body frame houses circuit

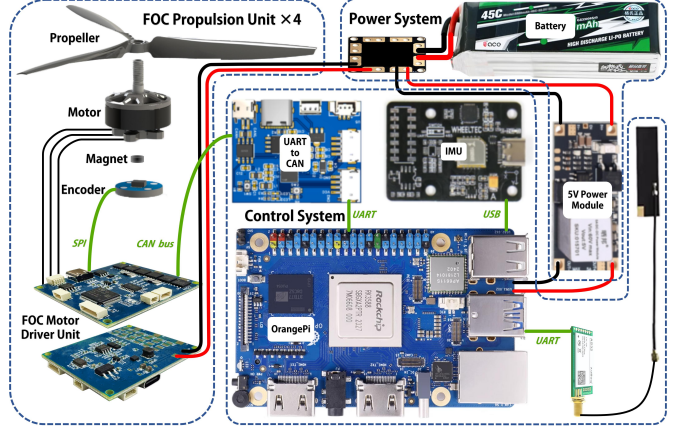


Fig. 4. The electronic equipment of the TriphiBot. The propulsion system consists of four FOC propulsion units.

modules including the onboard computer and motor drivers, while the lower section contains the IMU unit and the battery. The layout of the above components causes the CoG of the robot to shift in the positive direction of the  $x_b$  axis of the body. However, due to the balanced mass on the upper and lower sides in the  $y_b$  axis direction, the CoG does not shift in this direction, thus forming a triphibious robot platform with eccentric CoG characteristics. To allow the robot work in water, the printed circuit boards are protected with a coating of KAFUTER 704 silicone sealant and UV-cured glue. This treatment provides effective waterproofing and dustproofing while maintaining adequate heat dissipation. Note that the TriphiBot is designed with negative buoyancy. The buoyancy center of robot is vertically aligned with the CoG, and it is slightly higher than the CoG.

### B. FOC based Unified Propulsion System

The different physical characteristics and different motion modes place distinct requirement for the drive system for a triphibious robot across air, land, and water. The motor should be capable of high torque at low speed underwater, extremely high speed in flight, and good control performance close to zero-speed rotation to generate flexible bidirectional thrust on the ground. We employ the FOC technology to control the motors by separately installing encoders on the back of motor. Then we can generate precise rotating magnetic fields based on the position of the motor axis. It has been proven in existing literature that FOC outperforms open-loop control and estimated rotational speed feedback control in controlling the motor during high-speed rotation in the air [22]. The full-stack control architecture for triphibious motion control is described in Section IV.

This propulsion system has the characteristics of a compact structure, light weight, and high output power, as shown in Fig. 4. The system includes four FOC motor driver units, which are designed and optimized based on the VESC<sup>1</sup> open-source project [23]. The driver utilizes an STM32F405RG76 control chip operating at up to 168 MHz to execute the core

<sup>1</sup><https://vesc-project.com/>

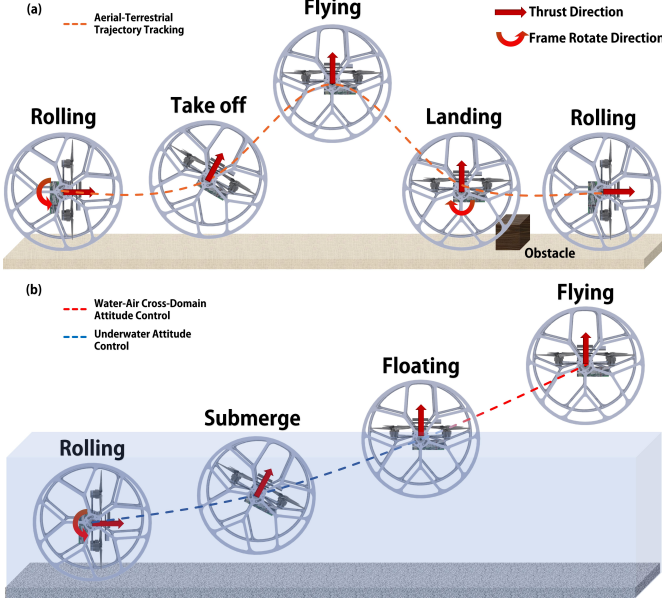


Fig. 5. Conceptual diagram of cross-domain transitions. (a) After changing the body's attitude, robot takes off, flies and lands, including crossing obstacles by changing the attitude. (b) From the seabed to the air.

VESC algorithm. It receives speed commands via a CAN bus and employs MOSFETs with a maximum operating voltage of 60 V and a maximum current of 170 A. To achieve a high-precision closed-loop motor control system, the AS5047P high-resolution rotational position sensor is used as the feedback element. This sensor is suitable for measuring speeds up to 28,000 RPM and can read 14-bit absolute angle information through the 4-wire SPI interface, providing accurate position feedback for the FOC algorithm.

The drive circuit board weighs only 12.5g, similar to the ESC circuit board, achieving a high ratio of thrust to weight. This propulsion system exhibits outstanding dynamic performance, with a maximum speed of up to 200,000 electrical revolutions per minute(eRPM) and the ability to quickly switch the rotation direction. Its control performance at low speeds is superior to that of traditional ESCs, enabling precise and smooth torque control. The control parameters have been adjusted for the new MOSFET and other components, and the motor parameters have been automatically identified and configured with the help of the VESC software tool, further enhancing the system's adaptability and debugging efficiency.

### C. System Electronic Design

The electronic equipment system architecture of the robot is shown in Fig. 4. Given the significant differences in power requirements and working characteristics of different components, this design adopts a distributed power supply scheme. Specifically, considering that the FOC motor propulsion system needs a large current and there is a risk of reverse electromotive force, it is directly connected to a GREPOW 4S 3300mAh 45C high-rate lithium battery. The main control board and other low-power devices are powered by a dedicated DC-DC 5V voltage regulator module.

We eliminate the need for a separate flight controller by using an interface-rich OrangePi 5 Max as the main control board, which directly reads external IMU data via serial communication. Due to the strong attenuation of electromagnetic waves in water, we employ a dual-band communication strategy: an onboard 5GHz WiFi module for aerial operations and a 433MHz module (AS32-TTL-1W) for underwater environment. Control instructions from the main board are transmitted via the serial port to a custom STM32F4 protocol conversion board. Following protocol conversion, speed control signals are distributed to each motor driver unit via the CAN bus.

### III. DYNAMIC MODEL

This section begins with an analysis of the dynamics of TriphiBot in different motion modes, followed by a derivation of its differential flatness properties in aerial and terrestrial mode.

#### A. Triphibious Motion Mode Dynamics

We categorize it into flight mode (in air or water) and ground mode (on land or seabed) based on whether TriphiBot contacts the supporting surface, as shown in Fig. 3(b). In the flight mode and the ground mode, the plane  $x_A O_A y_A$  are horizontal and vertical, respectively.

We use  $\zeta$  as the environment medium state flag, where  $\zeta = 1$  and 0 represent the robot's presence in water and in the air, respectively. For underwater robots, added mass is the additional mass that a robot appears to have when it is accelerated or decelerated relative to the surrounding fluid. We define the added mass and the added inertial matrix as  $m_a$  and  $M_a$  respectively. Meanwhile, the robot will be affected by water resistance and drag moment, which can be expressed as

$$f_{drag} = C_f \|v_A\|v_A, \tau_{drag} = C_t \|\omega_A\|\omega_A, \quad (1)$$

where  $C_f$  is the drag coefficient,  $C_t$  is the drag moment coefficient. When TriphiBot dives into the water, it is subjected to the buoyancy force, which is given by

$$\mathbf{F}_B = \rho_w V \mathbf{g}, \quad (2)$$

where  $\rho_w$  is the density of water,  $V$  is the volume of displaced water, and  $\mathbf{g} = [0, 0, g]^\top$ .

The above parameters can be determined through manual adjustments in the experiment or by using system identification methods.

1) *Flight Mode*: In the flight mode, we conduct the analysis using the coordinate system  $\mathcal{F}_A$ . The position vector in  $\mathcal{F}_W$  is defined as  $\mathbf{p}_W = [p_{W,x}, p_{W,y}, p_{W,z}]^\top$ , and the attitude vector is  $\Theta_A = [\phi_A, \theta_A, \psi_A]^\top$ . In coordinate system  $\mathcal{F}_A$ , the velocity and angular rate vector are  $\mathbf{v}_A = [v_{A,x}, v_{A,y}, v_{A,z}]^\top$  and  $\mathbf{w}_A = [w_{A,x}, w_{A,y}, w_{A,z}]^\top$ , respectively.  $\mathbf{R}_A^W$  defined as the rotation matrix that represents the transformation from  $\mathcal{F}_A$  to  $\mathcal{F}_W$  is given by

$$\mathbf{R}_A^W = \begin{bmatrix} c\theta c\psi & s\phi s\theta c\psi - c\phi s\psi & c\phi s\theta c\psi + s\phi s\psi \\ c\theta s\psi & s\phi s\theta s\psi + c\phi c\psi & c\phi s\theta s\psi - s\phi c\psi \\ -s\theta & s\phi c\theta & c\phi c\theta \end{bmatrix}, \quad (3)$$

and the transformation matrix of angular rate  $\mathbf{W}$  is given by

$$\mathbf{W} = \begin{bmatrix} 1 & s\phi t\theta & c\phi t\theta \\ 0 & c\phi & -s\phi \\ 0 & s\phi/c\theta & c\phi/c\theta \end{bmatrix}, \quad (4)$$

where  $c(\cdot)$ ,  $s(\cdot)$  and  $t(\cdot)$  represent the abbreviation of  $\cos(\cdot)$ ,  $\sin(\cdot)$  and  $\tan(\cdot)$ . The  $\phi$ ,  $\theta$  and  $\psi$  is  $\phi_A$ ,  $\theta_A$  and  $\psi_A$ . The TriphiBot's kinematic equations of flight mode can be expressed as

$$\dot{\mathbf{p}}_W = \mathbf{R}_A^W \mathbf{v}_A, \dot{\Theta}_A = \mathbf{W} \boldsymbol{\omega}_A. \quad (5)$$

The dynamic equations are given by

$$\begin{aligned} (m + \zeta m_a) \dot{\mathbf{v}}_A &= -(m + \zeta m_a) \mathbf{v}_A \times \boldsymbol{\omega}_A + T \mathbf{z}_A \\ &\quad - \mathbf{R}_A^{W^\top} (m + \zeta m_a) \mathbf{g} - \zeta \mathbf{f}_{drag} \\ &\quad + \zeta \mathbf{R}_A^{W^\top} \mathbf{F}_B, \\ (\mathbf{M}_A + \zeta \mathbf{M}_a) \dot{\boldsymbol{\omega}}_A &= \boldsymbol{\tau}_A - \boldsymbol{\omega}_A \times (\mathbf{M}_A + \zeta \mathbf{M}_a) \boldsymbol{\omega}_A \\ &\quad - \zeta \boldsymbol{\tau}_{drag}, \end{aligned} \quad (6)$$

where  $m$  is the total mass of the robot and the matrix  $\mathbf{M}_A = \text{diag}[M_{A,xx}, M_{A,yy}, M_{A,zz}]$  represents moment of inertia tensor defined at the CoG.  $\times$  is the cross product and  $T$  is collective rotor thrust.  $\boldsymbol{\tau}_A = [\tau_{A,x}, \tau_{A,y}, \tau_{A,z}]^\top$  is control torque, and because of its asymmetric design it can be expressed as

$$\begin{bmatrix} T \\ \tau_{A,x} \\ \tau_{A,y} \\ \tau_{A,z} \end{bmatrix} = \begin{bmatrix} 1 & 1 & 1 & 1 \\ -\frac{\lambda}{\sqrt{2}} & \frac{\lambda}{\sqrt{2}} & \frac{\lambda}{\sqrt{2}} & -\frac{\lambda}{\sqrt{2}} \\ \delta - \frac{\lambda}{\sqrt{2}} & \frac{\lambda}{\sqrt{2}} + \delta & \delta - \frac{\lambda}{\sqrt{2}} & \frac{\lambda}{\sqrt{2}} + \delta \\ -\frac{c_m}{c_t} & -\frac{c_m}{c_t} & \frac{c_m}{c_t} & \frac{c_m}{c_t} \end{bmatrix} \mathbf{u}, \quad (8)$$

where  $\lambda$  is the arm length,  $\delta$  is the distance from the centroid to the CoG and  $\mathbf{u} = [T_1, T_2, T_3, T_4]^\top$  is the thrust of each motor.  $c_m$  and  $c_t$  are the rotor torque and thrust coefficient, respectively. Note that  $c_t$  is separately divided into  $c_{t,w}$  in water and  $c_{t,a}$  in air, and is classified as  $c_{t,w}^f, c_{t,w}^r, c_{t,a}^f, c_{t,a}^r$ , according to the direction of the thrust.

2) *Ground Mode*: In the ground mode, we assume that the ground surface is flat and there is no lateral movement of the wheels. For the convenience of analysis, we conduct the analysis using the coordinate system  $\mathcal{F}_T$ .  $\mathcal{F}_T$  is obtained by rotating  $\mathcal{F}_A$  90 degrees in the positive direction of  $\mathbf{y}_A$ . The attitude and angular rate vector are  $\boldsymbol{\Theta}_T = [\phi_T, \theta_T, \psi_T]^\top$  and  $\boldsymbol{\omega}_T = [\omega_{T,x}, \omega_{T,y}, \omega_{T,z}]^\top$ , respectively. The kinematic equations of ground mode are given by

$$\dot{\mathbf{p}}_W = [v_l \cos \psi_T, v_l \sin \psi_T, 0]^\top, \quad (9)$$

$$\dot{v}_l = \frac{T \cos \theta_T - \zeta \| \mathbf{f}_{drag} \|}{(m + \zeta m_a)}, \quad (10)$$

where  $v_l$  is a scalar quantity representing the speed on a horizontal plane. The dynamic equations are given by

$$\dot{\boldsymbol{\Theta}}_T = [\dot{\phi}_T, \dot{\theta}_T, \dot{\psi}_T]^\top = [0, w_{T,y}, w_{T,z} \sec \theta_T]^\top, \quad (11)$$

$$\begin{aligned} \dot{\boldsymbol{\omega}}_T &= (\mathbf{M}_T + \zeta \mathbf{M}_a)^{-1} (\boldsymbol{\tau}_T - \boldsymbol{\omega}_T \times (\mathbf{M}_T + \zeta \mathbf{M}_a) \boldsymbol{\omega}_T \\ &\quad - \boldsymbol{\tau}_g - \zeta (\boldsymbol{\tau}_{buo} + \boldsymbol{\tau}_{drag})), \end{aligned} \quad (12)$$

where  $\mathbf{M}_T = \text{diag}[M_{T,xx}, M_{T,yy}, M_{T,zz}]$  represents moment of inertia tensor defined at the geometric center,  $\boldsymbol{\tau}_{buo}$  is the

buoyancy moment vector,  $\boldsymbol{\tau}_g = [0, m\|\mathbf{g}\|\delta \sin \theta_T, 0]^\top$  is the gravity moment vector, and  $\boldsymbol{\tau}_T = [\tau_{T,x}, \tau_{T,y}, \tau_{T,z}]^\top$  is the control moment vector and it can be expressed as

$$\begin{bmatrix} T \\ \tau_{T,x} \\ \tau_{T,y} \\ \tau_{T,z} \end{bmatrix} = \begin{bmatrix} 1 & 1 & 1 & 1 \\ -\frac{\lambda}{\sqrt{2}} & \frac{\lambda}{\sqrt{2}} & \frac{\lambda}{\sqrt{2}} & -\frac{\lambda}{\sqrt{2}} \\ -\frac{\lambda}{\sqrt{2}} & \frac{\lambda}{\sqrt{2}} & -\frac{\lambda}{\sqrt{2}} & \frac{\lambda}{\sqrt{2}} \\ -\frac{c_m}{c_t} & -\frac{c_m}{c_t} & \frac{c_m}{c_t} & \frac{c_m}{c_t} \end{bmatrix} \mathbf{u}. \quad (13)$$

To sum up, the state vector of the hybrid system is  $\mathbf{X} = [\mathbf{p}_W^\top, \mathbf{v}_A^\top, \boldsymbol{\Theta}_A^\top, \theta_T, \psi_T, \mathbf{w}_A^\top, \mathbf{w}_T^\top, v_l]^\top$  and the input vector is  $\mathbf{u} = [T_1, T_2, T_3, T_4]^\top$ .

### B. Differential Flatness

When the robot is in aerial flight mode, based on the analysis of the CoG, it can be regarded as a regular quadcopter. The differential flatness of the quadcopter in the aerial mode has been well studied in previous works [24], [25], [26], [27], where the flat output is selected as  $\boldsymbol{\sigma}_f = [p_{W,x}, p_{W,y}, p_{W,z}, \psi_A]^\top$ . The state and input vectors are  $\mathbf{X}_a = [\mathbf{p}_W^\top, \mathbf{v}_A^\top, \boldsymbol{\Theta}_W^\top, \boldsymbol{\omega}_A^\top]^\top$  and  $\mathbf{u} = [T_1, T_2, T_3, T_4]^\top$ , respectively.

When the robot contacts the ground, we define the flat output of terrestrial mode as  $\boldsymbol{\sigma}_t = [p_{W,x}, p_{W,y}, \theta_T]^\top$ . In order to prove the differential flatness on the land, we need to derive each state and input in  $\mathbf{X}_t = [\mathbf{p}_W^\top, v_l, \theta_T, \psi_T, \boldsymbol{\omega}_T^\top]^\top$  and  $\mathbf{u} = [T_1, T_2, T_3, T_4]^\top$  from  $\boldsymbol{\sigma}_t$  and its derivatives. As we assume that the robot is not skidding on the land, the  $\psi_T$  value is given as

$$\psi_T = \arctan 2(\kappa \dot{p}_{W,y}, \kappa \dot{p}_{W,x}), \quad (14)$$

where  $\kappa$  represents the direction of the robot's movement (when  $\kappa = 1$ , it moves forward, when  $\kappa = -1$ , it moves backward). We can directly get  $\mathbf{p}_W$  and  $\theta_T$  from  $\boldsymbol{\sigma}_t$  and we do not want it to rotate around the  $\mathbf{x}_T$ . Therefore, we expect  $\tau_{T,x} = 0$  and we can get  $\boldsymbol{\omega}_T$  from  $\theta_T$  and  $\psi_T$ .

$$\boldsymbol{\omega}_T = \begin{bmatrix} -\sin \theta_T \dot{\psi}_T \\ \dot{\theta}_T \\ \dot{\psi}_T \cos \theta_T \end{bmatrix}, \dot{\boldsymbol{\omega}}_T = \begin{bmatrix} -\cos \theta_T \dot{\theta}_T \dot{\psi}_T - \sin \theta_T \ddot{\psi}_T \\ \ddot{\theta}_T \\ \ddot{\psi}_T \cos \theta_T - \dot{\psi}_T \dot{\theta}_T \sin \theta_T \end{bmatrix}. \quad (15)$$

$v_l$  is given by

$$v_l = \kappa \sqrt{(\dot{p}_{W,x})^2 + (\dot{p}_{W,y})^2}. \quad (16)$$

To maximize energy efficiency, we keep  $x_T$  parallel to the land, namely  $\theta_T = 0$ . By substituting (16) into (10), the total thrust  $T$  is given by

$$T = m \dot{v}_l = \frac{m(\ddot{p}_{W,x} \dot{p}_{W,x} + \ddot{p}_{W,y} \dot{p}_{W,y})}{\cos \theta_T \sqrt{(\dot{p}_{W,x})^2 + (\dot{p}_{W,y})^2}}. \quad (17)$$

Then by combining (12), (15), we can get  $\boldsymbol{\tau}_T$ . Finally, we obtain  $\mathbf{u}$  with  $T$  and  $\boldsymbol{\tau}_T$  substituted into the inverse form of (13). All the variables of state  $\mathbf{X}_t = [\mathbf{p}_W^\top, v_l, \theta_T, \psi_T, \boldsymbol{\omega}_T^\top]^\top$  and input  $\mathbf{u} = [T_1, T_2, T_3, T_4]^\top$  can be obtained from the flat output. Therefore, we can conclude that the terrestrial dynamics of TriphiBot is differentially flat.

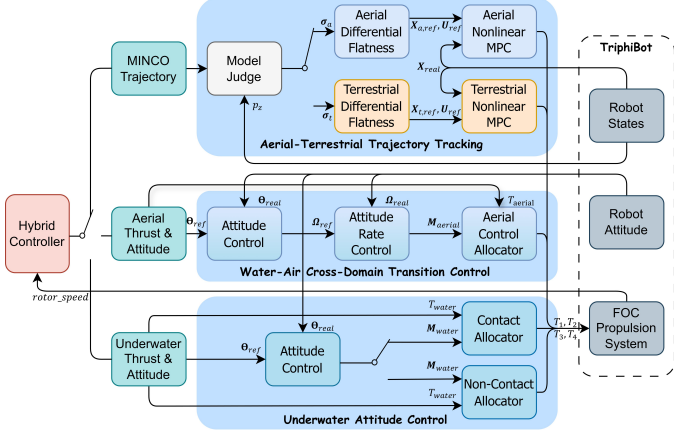


Fig. 6. The hybrid control structure of TriphiBot. The controller automatically determines the switching variable  $\eta$  based on the reference height  $p_z$ . The transitions are accomplished within a unified HNMPC framework. When transferring from water to the air or the land, it needs to be controlled through PID methods.

#### IV. CONTROL ARCHITECTURE AND MOTOR CONTROL

In this section, we introduce the cross-domain control framework of TriphiBot, and provide a detailed explanation of how the TriphiBot switches control methods when performing cross-domain, cross-mode tasks. Fig. 5 is a concept diagram for cross-domain transitions. Additionally, we describe how the FOC method of the motor can automatically adapt to the required working speed and torque.

## A. Hybrid Control Architecture

Since high-rate communication and precise positioning are accessible in the air but severely limited in underwater and air-water transition phases, we developed distinct control methods that are activated according to the operation mode. As shown in Fig. 6, we design a HNMPC-PID control system based on a finite state machine.

**Aerial-Terrestrial Trajectory Tracking.** For both aerial and terrestrial position control, we get a flat-output trajectory from MINCO [28], then derive the reference trajectory utilizing the differential flatness. We design an HNMPC controller, which accurately distinguishes the dynamic of robot by using discrete switching variable  $\eta$ . The controller automatically determines the switching variable  $\eta$  based on the reference  $p_z$ .

The HNMPC finds the best control commands by solving an optimal control problem(OCP) in a receding horizon manner. It aims to minimize the cost function of the error between the predicted state of measurement and the reference trajectory within the time range  $[t_0, t_0+h]$ . The time range is  $h = N \cdot dt$ , where  $dt$  represents the time step and  $N$  is the number of steps.

The aerial and terrestrial dynamics of the system is described as

$$f(\mathbf{x}, \mathbf{u}) = \eta f(\mathbf{x}_t, \mathbf{u}) + (1 - \eta) f(\mathbf{x}_a, \mathbf{u}). \quad (18)$$

Then, the NMPC problem is transformed into a nonlinear programming problem, and the optimal control command

sequence  $u^* \in \mathbb{R}^{4 \times N}$  is generated as

$$\begin{aligned}
\mathbf{u}^* = \min_{\mathbf{u}} \sum_{i=k}^{k+N-1} & [\eta \cdot \tilde{\mathbf{x}}_{t,i}^\top \mathbf{Q}_t \tilde{\mathbf{x}}_{t,i} \\
& + (1-\eta) \cdot \tilde{\mathbf{x}}_{a,i}^\top \mathbf{Q}_a \tilde{\mathbf{x}}_{a,i} + \tilde{\mathbf{u}}_i^\top \mathbf{Q}_u \tilde{\mathbf{u}}_i] \\
& + \eta \cdot \tilde{\mathbf{x}}_{t,N}^\top \mathbf{Q}_t \tilde{\mathbf{x}}_{t,N} + (1-\eta) \tilde{\mathbf{x}}_{a,N}^\top \mathbf{Q}_a \tilde{\mathbf{x}}_{a,N}, \\
\text{s.t. } & \mathbf{x}_{i+1} = f(\mathbf{x}_i, \mathbf{u}_i), \mathbf{u}_i \in [\mathbf{u}_{min}, \mathbf{u}_{max}],
\end{aligned} \tag{19}$$

where  $\eta$  is the discrete variable, which is given by

$$\eta = \begin{cases} 1, & \text{if } p_{W,z,k} < h_{judge} \\ 0, & \text{if } p_{W,z,k} > h_{judge} \end{cases}, \quad (20)$$

where  $h_{judge}$  is threshold used to determine whether to take off.  $k$  is the current time step,  $\tilde{x}_{t,i} = \mathbf{x}_{t,ref} - \mathbf{x}_{t,i}$ ,  $\tilde{x}_{a,i} = \mathbf{x}_{a,ref} - \mathbf{x}_{a,i}$  and  $\tilde{u}_i = \mathbf{u}_{ref,i} - \mathbf{u}_i$  are the terrestrial states, aerial states and inputs error, respectively.  $\tilde{x}_{t,k+N}$  and  $\tilde{x}_{a,k+N}$  are the end states error.  $\mathbf{Q}_t$ ,  $\mathbf{Q}_a$  and  $\mathbf{Q}_u$  are the terrestrial states, aerial states and inputs weight matrix written as

$$\mathbf{Q}_t = \text{diag} ([\mathbf{Q}_p, \mathbf{Q}_w, Q_{vl}, Q_\theta, Q_\psi]), \quad (21)$$

$$\mathbf{Q}_a = \text{diag} ([\mathbf{Q}_p, \mathbf{Q}_v, \mathbf{Q}_\Theta, \mathbf{Q}_w]), \quad (22)$$

$$\mathbf{Q}_u = \text{diag} ([Q_{T_1}, Q_{T_2}, Q_{T_3}, Q_{T_4}]) . \quad (23)$$

**Water-Air Cross-Domain transition Control.** Since the positioning of the robot from water to air cannot be seamless, and waves can affect the stability of positioning as robot floats on the water, we use cascade PID control for cross-domain transition control when it jumps out of the water. In the aerial attitude controller, the inner loop tracks angular velocity, while the outer loop tracks angle. Then, the control allocator maps the required torque into the required thrust  $u$  according to (8).

When the robot jumps out of the water, the rotational speed of rotors increases to tens of thousands of RPM. Conversely, upon water entry, the speed drops rapidly to a few hundred RPM. The hybrid controller determines whether the robot has left the water surface by monitoring the changes in the rotor speed, and then triggers the corresponding controller. When the robot is out of the water and its attitude is stable, it can switch to trajectory tracking mode.

**Underwater attitude Control.** For underwater control, since it is difficult to obtain precise positioning and smooth communication, we employ attitude control. The control law for the angle loop is formulated as follows:

$$e_{\Theta} = \Theta_{des} - \Theta = \begin{bmatrix} \phi_{des} - \phi \\ \theta_{des} - \theta \\ \psi_{des} - \psi \end{bmatrix}, \quad (24)$$

$$\tau_{des} = K_p^\Theta e_\Theta + K_i^\Theta \int e_\Theta dt + K_d^\Theta \dot{e}_\Theta. \quad (25)$$

Among them,  $K_p^\Theta, K_i^\Theta, K_d^\Theta$  are the proportional, integral, and derivative components of the angle control for the diagonal gain matrix.  $\tau_{des}$  is three-axis control torque. Afterward, when the robot is operating in water, thrust  $u$  is calculated using (8), and when it is on the seabed, thrust  $u$  is calculated using (13). It is also worth noting that  $c_t$  should be changed to the underwater thrust coefficient  $c_w$ .

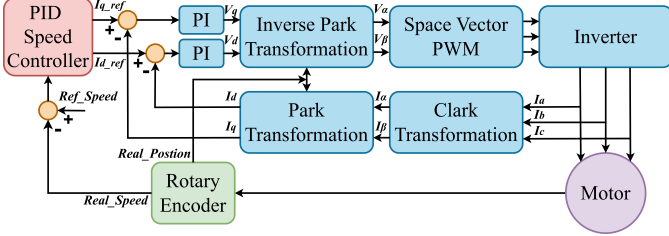


Fig. 7. The FOC algorithm, in which  $I_{q\_ref}$  determines the motor torque. This algorithm adjusts the current  $I_{q\_ref}$  based on the rotational speed error to achieve torque matching. The current  $I_{d\_ref}$  is usually set to 0.

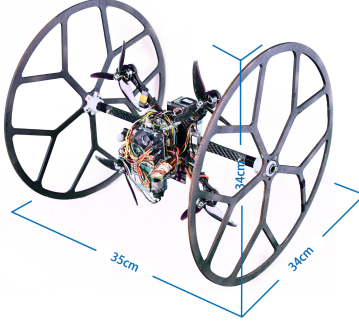


Fig. 8. The prototype of TriphiBot in its ground-stable state.

### B. Motor Control

We adopt the FOC technology with an encoder to control the motor speed. By installing a magnet at the bottom of the motor, the encoder can feedback the precise motor position. Then, we can control the magnetic field direction based on the position, ensuring it remains perpendicular to the rotor's permanent magnetic field. This ensures that the maximum torque is generated under a given current. To achieve precise speed regulation of motor, FOC typically employs a cascaded control structure consisting of an inner current loop and an outer speed loop, both implemented via PID algorithms. Fig. 7 presents the flowchart of the FOC algorithm. The FOC current controller in this figure is similar to the standard FOC current control method [29]. In this figure, the rotational torque of the motor is determined based on the reference current  $I_{q\_ref}$ , and  $I_{d\_ref}$  is usually set to 0. When the motor operates in water and the rotational speed fails to reach the desired value, the PID algorithm will increase the reference current  $I_{q\_ref}$  to achieve adaptive torque matching.

## V. EXPERIMENT

In this section, we set up a test bench to evaluate the propulsion capability of the propulsion unit through static output characteristics. Meanwhile, we conduct a comprehensive validation of the TriphiBot's motion and cross-domain capability through trajectory tracking, attitude control, and cross-domain transition experiments across aerial, terrestrial and aquatic environments.

### A. Experiments Setup

The prototype of TriphiBot is designed and developed as shown in the Fig. 8. The physical parameters and controller

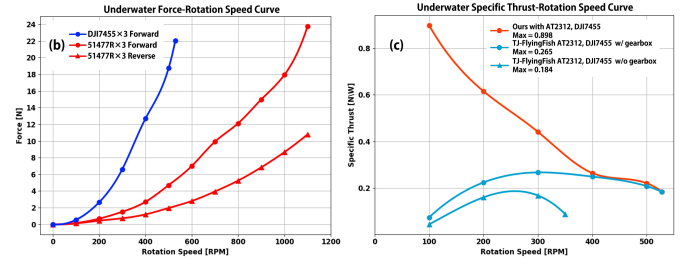
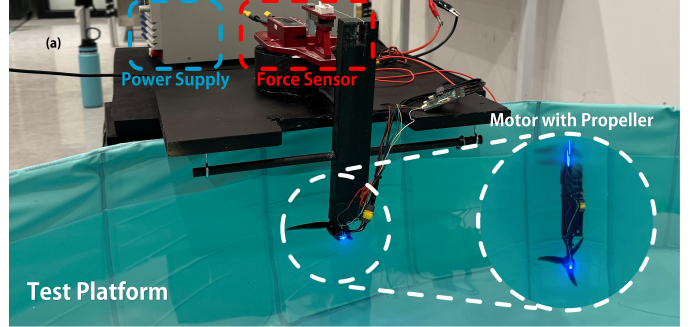


Fig. 9. The static performance testing of the propulsion system: (a) Test Platform. (b) The underwater force-rotation speed curves of different propellers. (c) The underwater specific thrust-rotation speed curves compared with TJ-FlyingFish.

parameters are listed in the Table I. The global localization when testing with controller is obtained from the NOKOV<sup>2</sup> motion capture system. We solve the NMPC problem using ACADO toolkit [30] and qpOASES [31], with a control frequency of 200Hz. We use the root-mean-square error (RMSE) to evaluate the tracking performance, which is expressed as

$$\text{RMSE} = \sqrt{\frac{1}{N} \sum_{k=1}^N \|\mathbf{p}^k - \mathbf{p}_{\text{ref}}^k\|}. \quad (26)$$

Among them,  $\mathbf{p}^k$  and  $\mathbf{p}_{\text{ref}}^k$  represent the actual and reference position sampled at the  $k$ -th step respectively.

### B. Output Characteristics of the Propulsion System

We validate the proposed propulsion unit's performance through a series of tests in this section. As shown in Fig. 9(a), the dedicated experimental platform set up for performance testing of propulsion unit is composed of a power supply and a force sensor.

**Rapid forward/backward thrust switching.** First, a rapid forward/backward thrust switching experiment is conducted in the air with the propeller installed on the motor. We also adopt a closed-loop speed control using a ESC with the same motor and propeller for comparison. The target speed in the experiment is set to 2100 RPM and the experimental results are shown in Fig. 10(a). Under such a high-frequency switching requirement, the traditional ESC with closed-loop control can only effectively track switching signals with a 0.5s interval, and there is also a steady-state error. In contrast, the proposed propulsion unit performs much better and is capable of tracking switching signals with a 0.25s interval.

<sup>2</sup><https://www.nokov.com/>

The response curve is smooth, with almost no overshoot observed. This result proves the superiority of our propulsion unit in dynamic response performance.

**Precise speed control underwater.** We test the mapping relationship between the different rotational speeds and corresponding underwater thrust outputs for different propellers (DJI7455 $\times$ 3 and 51477R $\times$ 3). The experimental data shown in Fig. 9(b) indicate that the rotor's operational speed underwater, in both directions, is confined to a 0-1200 RPM range, markedly lower than that measured in air. This also demonstrates that the underwater thrust  $T$  relates to the rotational speed  $\omega$  by  $T = c_a \omega^2$ .

**Fast startup underwater.** In terms of dynamic response characteristics, Fig. 10(b) presents the comparative experimental results of the motor startup process. We set the underwater target rotational speed at 420 RPM, and it can be observed that the motor controlled by the ESC exhibits oscillation during the startup stage and has obvious steady-state error. In contrast, the proposed propulsion unit demonstrates excellent dynamic performance. It reaches 90% of the expected speed in approximately 0.14s, with a smooth and rapid transition. Its control accuracy and response speed are superior to the ESC.

**Underwater high-efficiency verification.** To quantitatively evaluate the underwater energy efficiency advantages of the proposed motor driver, we conduct a comparative test of power consumption and specific thrust at different rotational speeds. The experimental results Fig. 11(a) clearly show that, throughout the entire test speed range, the power consumption of the ESC is much higher than ours. Among them, the ESC's maximum power consumption reaches up to five times that of our driver. In terms of specific thrust, as shown in Fig. 11(b), our propulsion unit achieves a value of up to 0.825N/W, a performance level 14 times greater than the traditional ESC's 0.059N/W. The test results further show that the ESC is incapable of providing adequate torque for the underwater load due to its control strategy, thus operating at extremely low efficiency. This restricts its maximum speed to only 700 RPM under the maximum allowable continuous current.

**Verification of Driver Compatibility.** When the torque output of a brushless motor is inadequate, meaning torque matching is not accomplished, a decrease in its specific thrust results. We apply our driver to the same motor and propeller as the TJ-FlyingFish [15] (T-MOTOR AT2312-KV1150 motor and DJI9455 $\times$ 3 propeller) to demonstrate its compatibility, and compare its specific thrust performance against the mechanical design used by TJ-FlyingFish. The experimental results Fig. 9(c) show that the underwater specific thrust achieved by ours is superior to the comparison scheme. The maximum specific thrust in TJ-FlyingFish is 0.265N/W, while ours can reach 0.898N/W under the same conditions, with a performance improvement. This result demonstrates that our driver can effectively adapt to different types of motor and propeller combinations.

### C. Aerial Experiment

Considering the fact that it is similar to a standard drone in the air, we simplify the experiment for the purely aerial test.

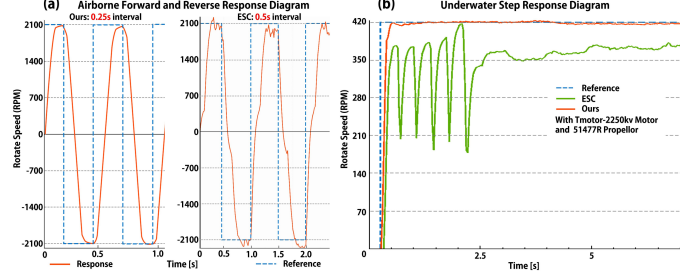


Fig. 10. (a) The response of the rotor to high-speed forward and backward rotation in air using different drivers. (b) The underwater step response with different drivers.

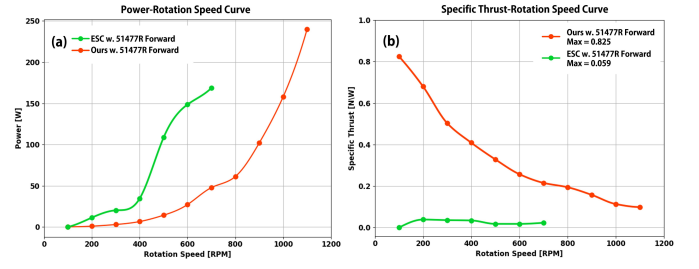


Fig. 11. (a) The underwater power-rotation speed curves of different drivers. (b) The underwater specific thrust-rotation speed curves of different drivers.

We evaluate the aerial maneuverability of TriphiBot through a flight test involving takeoff and accurate tracking of an 8-shaped trajectory. The robot performed this task at a maximum speed of 2m/s and acceleration of 2m/s<sup>2</sup>. The trajectory tracking result is shown in Fig. 12(a), with RMSE of 0.096m. This experiment indicates that by incorporating the CoG shift into the model, excellent control results can be achieved.

### D. Terrestrial Experiment

In the terrestrial mode, like Lai et al. [14], we keep the pitch angle  $\theta_T$  constant at 0° and track an 8-shaped trajectory in order to maximize the energy utilization. As shown in Fig. 12(b), the maximum speed and acceleration reached 3m/s and 2.5m/s<sup>2</sup>, respectively, with a trajectory tracking RMSE of 0.074m. To compare the stability in the terrestrial mode, we measure the pitch angle from a part of the trajectory, indicated by the green dashed rectangle in the Fig. 12(b). We plot our result with the result from Zhang et al. [13] and Lai et al. [14] in Fig. 13(a). The pitch angle fluctuation of our robot is within small range from -4.41° to 2.51°, compared to -2.2° to 9.9° for Lai's experiment and a much wider -12.6° to 62.3° for the Zhang's experiment. This result demonstrates that the designed CoG shift, coupled with precise thrust control of our propulsion unit, enables a more stable attitude control during high-speed terrestrial travel.

Due to a 90° rotation around the  $y_t$  axis when transitioning from flight to terrestrial mode, the robot's ground clearance is significantly reduced from 11 cm to just 2 cm. The control performance of our propulsion system enables robot to be manipulated at any pitch angle during ground rolling, allowing it to overcome obstacles. We design an experiment to verify that the robot has good passability. In Fig. 14(c), we can see

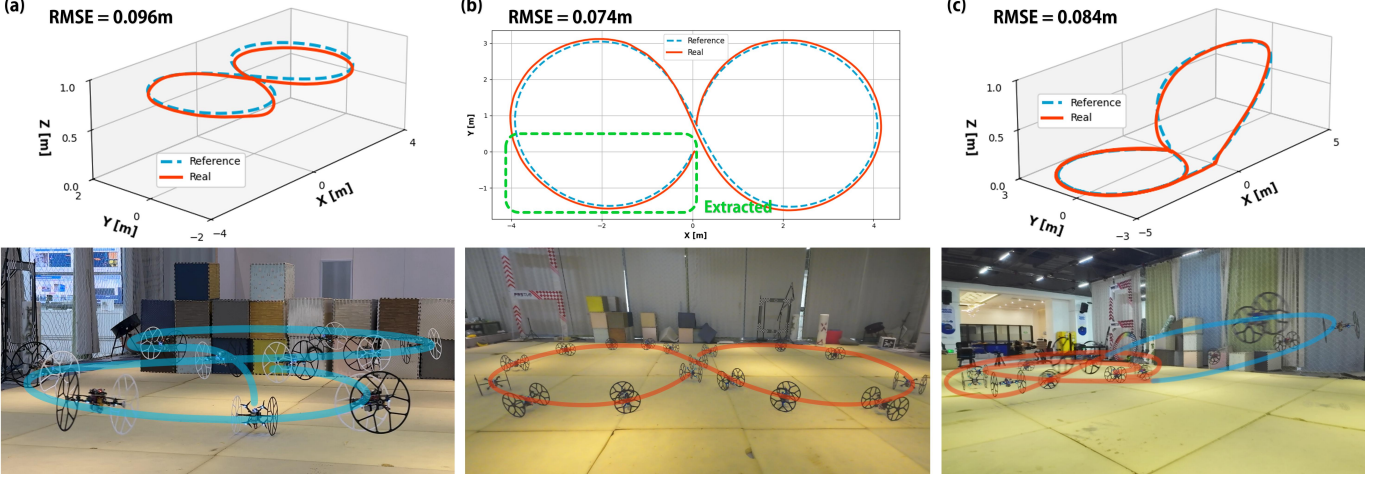


Fig. 12. (a) Reference and real  $p_{W,xyz}$  when tracking an 8-shaped aerial trajectory. (b) Reference and real  $p_{W,xy}$  when tracking an 8-shaped terrestrial trajectory, the green dashed rectangular box indicates the extracted section of the trajectory. (c) Reference and real  $p_{W,xyz}$  when tracking an 8-shaped aerial-terrestrial trajectory.

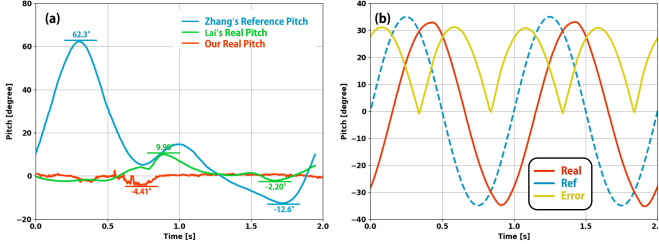


Fig. 13. (a) Our real  $\theta_T$ , TrofyBot's real  $\theta_T$  and reference  $\theta_T$  of Zhang's reference trajectory from the terrestrial extracted section. (b) The test results of tracking sinusoidal attitude signal and the absolute value of the error.

that by controlling  $\theta_T$  to improve ground clearance, the robot successfully crosses a ground obstacle with a height of 9cm.

#### E. Underwater Experiment

Underwater vehicles are characterized by highly nonlinear dynamics, significant hydrodynamic damping, and added mass effects, which introduce large inertia and response delays. In this section, we demonstrate the underwater attitude control capability to verify that the proposed propulsion system can be effectively applied to the underwater vehicles. Fig. 14(a) shows the horizontal movement pattern of the robot on the bottom of the tank ( $3m \times 2m \times 0.6m$ ) to simulate the seabed. Considering the frequent dynamic changes of the pitch angle in the underwater environment, we conduct a pitch angle sinusoidal trajectory tracking test. The sinusoidal signal with a period of 1s and an amplitude of  $35^\circ$  is set as the target trajectory. The experimental results are shown in Fig. 13(b). The maximum error generated during the tracking process is  $31^\circ$ , and the phase lag time is only 0.17s. By comparison, Liu et al. [32] conducted the same tracking test of the Wukong, where they use ESCs combined with dedicated underwater motors and propellers as the propulsion scheme and introduce the INDI control algorithm to improve the robot's response performance. However, their maximum tracking error is larger

TABLE I  
TABLE OF PARAMETERS

Physical	Value	MPC	Value
$Size(L \times W \times H)[cm]$	$35 \times 34 \times 34$	$N, dt$	40, 0.05
$m[kg]$	1.1	$Q_p$	$diag(5000, 5000, 3000)$
$M_A[g \cdot m^2]$	$diag(0.0113, 0.0018, 0.0125)$	$Q_v$	$diag(500, 500, 500)$
$M_T[g \cdot m^2]$	$diag(0.0125, 0.0018, 0.0113)$	$Q_\theta$	$diag(500, 500, 500)$
$c_m[N \cdot m \cdot s^2]$	$2.56e^{-10}$	$Q_w$	$diag(10, 10, 10)$
$c_{t,f}, c_{t,r}[N \cdot s^2]$	$1.6e^{-8}, 7.79e^{-9}$	$Q_u$	$diag(100, 100, 100, 100)$
$c_{w,f}, c_{w,r}[N \cdot s^2]$	$1.83e^{-5}, 8.68e^{-6}$	$Q_{v_1}$	500
$\lambda, \delta[cm]$	8, 1.5	$Q_\theta, Q_\psi$	500, 500

than  $35^\circ$ , and the phase lag is approximately 0.2s. The comparison results show that the TriphiBot exhibits higher accuracy and faster response speed in dynamic attitude tracking.

#### F. Cross-Domain Transition Capability Demonstration

To demonstrate the smooth air-land transitions, we first conduct a tracking experiment involving an 8-shaped trajectory in two domains. The robot moves a certain distance on the land, then changes its posture and takes off. After a period of flight, the robot begins to descend, land, and then return to its starting position. During testing, the robot autonomously switches between aerial and terrestrial modes based on its real-time altitude and pitch angle. The maximum speed and acceleration of this trajectory are  $2m/s$  and  $2m/s^2$ , respectively. The trajectory tracking result is shown in Fig. 12(c), with RMSE of 0.084m.

In addition, the robot's transition from air to water can be achieved simply by lowering the rotor speed to dive into the water. Considering the water causes resistance disturbances to the robot and its propellers, the difficulty of the water-air transitions lies in determining when to start the flight from the water surface to fly in the air. Fig. 14(b) shows the transition process from the water to the air. Initially, the robot floats on the water surface with a rotor speed of 1000 RPM. At  $t = 0s$ , the robot switches to PID aerial attitude control. As the propeller speed increases, the robot stabilizes its attitude and lifts off from the water surface. At  $t = 1.2s$ ,



Fig. 14. (a) The robot is moving forward underwater. (b) Taking off from the water until achieving stable flight. (c) By changing the pitch angle to overcome ground obstacles.

it completely detaches from the water surface. At  $t = 1.5s$ , with the flight attitude stabilized, it switches to the HNMPC control method for trajectory tracking. It only takes 1.5s for the robot to take off from the water and achieves stable flight. After taking off from the water, the robot maintains a stable attitude and successfully transitions to free flight. The above results validate TriphiBot's capability for smooth cross-domain transitions and seamless switching of control methods.

## VI. CONCLUSION

This paper presents a novel triphibious robot capable of aerial, terrestrial, and aquatic motion, by a minimalist design combining a quadcopter structure with two passive wheels, without extra actuators. By utilizing an eccentric CoG design and a unified FOC propulsion system, the robot achieves high efficiency and cross-domain transitions. A HNMPC-PID controller further ensures stable maneuverability across diverse domains. In subsequent research, factors such as water flow disturbances should be incorporated, along with more robust cross-domain position controllers, to achieve more accurate and flexible comprehensive working ability across all fields.

## REFERENCES

- [1] Zheng Zeng, Chenxin Lyu, Yuanbo Bi, Yufei Jin, Di Lu, and Lian Lian. Review of hybrid aerial underwater vehicle: Cross-domain mobility and transitions control. *Ocean Engineering*, 248:110840, 2022.
- [2] Jane Pauline Ramirez and Salua Hamaza. Multimodal locomotion: next generation aerial-terrestrial mobile robotics. *Advanced Intelligent Systems*, 7(7):2300327, 2025.
- [3] Arash Kalantari and Matthew Spenko. Design and experimental validation of hytaq, a hybrid terrestrial and aerial quadrotor. In *2013 IEEE International Conference on Robotics and Automation*, pages 4445–4450. IEEE, 2013.
- [4] Lei Li, Siqi Wang, Yiyuan Zhang, Shanyuan Song, Chuqian Wang, Shaochang Tan, Wei Zhao, Gang Wang, Wenguang Sun, Fuqiang Yang, et al. Aerial-aquatic robots capable of crossing the air-water boundary and hitchhiking on surfaces. *Science robotics*, 7(66):eabm6695, 2022.
- [5] Yiduo Zhu, Ziyi Guo, Tao Li, and Meiling Wang. Implementation and performance assessment of triphibious robot. In *2019 IEEE International Conference on Mechatronics and Automation (ICMA)*, pages 1514–1519. IEEE, 2019.
- [6] Ziyi Guo, Yiduo Zhu, Tao Li, Meiling Wang, Linsen Xu, and Yucheng Wang. Design and control research of a triphibious robot based on rotors. In *2018 IEEE 9th International Conference on Software Engineering and Service Science (ICSESS)*, pages 454–459. IEEE, 2018.
- [7] Nana Takahashi, Shuhei Yamashita, Yurina Sato, Yuta Kutsuna, and Manabu Yamada. All-round two-wheeled quadrotor helicopters with protect-frames for air-land-sea vehicle (controller design and automatic charging equipment). *Advanced Robotics*, 29(1):69–87, 2015.
- [8] Yi Sun, Youzhi Xu, Kaijie Lu, Pengfei Li, Huan Shen, Jiajun Xu, Yadong Gao, Qijun Zhao, and Aihong Ji. A transverse bi-rotor aerial-aquatic robot based on coupled vector power system. *IEEE/ASME Transactions on Mechatronics*, 2025.
- [9] Qifan Tan, Xinyu Zhang, Huaping Liu, Shuyuan Jiao, Mo Zhou, and Jun Li. Multimodal dynamics analysis and control for amphibious fly-drive vehicle. *IEEE/ASME Transactions on Mechatronics*, 26(2):621–632, 2021.
- [10] Hongyu Xu, Xiangming Zheng, Yu Wang, and Luwei Liao. Flybot: A dual active wheel hybrid land-air robot with five-link leg joints. *IEEE Robotics and Automation Letters*, 2024.
- [11] Junxiao Lin, Ruibin Zhang, Neng Pan, Chao Xu, and Fei Gao. Skater: A novel bi-modal bi-copter robot for adaptive locomotion in air and diverse terrain. *IEEE Robotics and Automation Letters*, 9(7):6392–6399, 2024.
- [12] Neng Pan, Jinqi Jiang, Ruibin Zhang, Chao Xu, and Fei Gao. Skywalker: A compact and agile air-ground omnidirectional vehicle. *IEEE Robotics and Automation Letters*, 8(5):2534–2541, 2023.
- [13] Ruibin Zhang, Junxiao Lin, Yuze Wu, Yuman Gao, Chi Wang, Chao Xu, Yanjun Cao, and Fei Gao. Model-based planning and control for terrestrial-aerial bimodal vehicles with passive wheels. In *2023 IEEE/RSJ International Conference on Intelligent Robots and Systems (IROS)*, pages 1070–1077. IEEE, 2023.
- [14] Mingwei Lai, Yuqian Ye, Hanyu Wu, Chice Xuan, Ruibin Zhang, Qiuyu Ren, Chao Xu, Fei Gao, and Yanjun Cao. Trofybot: A transformable rolling and flying robot with high energy efficiency. In *2025 IEEE International Conference on Robotics and Automation (ICRA)*, pages 4989–4995. IEEE, 2025.
- [15] Xuchen Liu, Minghao Dou, Dongyue Huang, Biao Wang, Jinqiang Cui, Qinyuan Ren, Lihua Dou, Zhi Gao, Jie Chen, and Ben M Chen. Tj-flyingfish: Design and implementation of an aerial-aquatic quadrotor with tiltable propulsion units. *arXiv preprint arXiv:2301.12344*, 2023.
- [16] Hamzeh Alzu'bi, Iyad Mansour, and Osamah Rawashdeh. Loon copter: Implementation of a hybrid unmanned aquatic-aerial quadcopter with active buoyancy control. *Journal of field Robotics*, 35(5):764–778, 2018.
- [17] Kecheng Qin, Wei Tang, Yiding Zhong, Yang Liu, Huxiu Xu, Pingan Zhu, Dong Yan, Huayong Yang, and Jun Zou. An aerial-aquatic robot with tunable tilting motors capable of multimode motion. *Advanced Intelligent Systems*, 5(11):2300193, 2023.
- [18] Guoming Chen, An Liu, Junhua Hu, Jinfu Feng, and Zongcheng Ma. Attitude and altitude control of unmanned aerial-underwater vehicle based on incremental nonlinear dynamic inversion. *IEEE Access*, 8:156129–156138, 2020.
- [19] Alexandre C Horn, Pedro M Pinheiro, Cesar B Silva, Armando Alves Neto, and Paulo LJ Drews-Jr. A study on configuration of propellers for multirotor-like hybrid aerial-aquatic vehicles. In *2019 19th International Conference on Advanced Robotics (ICAR)*, pages 173–178. IEEE, 2019.
- [20] Yu Herng Tan, Rob Siddall, and Mirko Kovac. Efficient aerial-aquatic locomotion with a single propulsion system. *IEEE Robotics and Automation Letters*, 2(3):1304–1311, 2017.
- [21] Aibin Zhu, Jiuyan Song, Ying Li, Mengke Wu, and Xiaodong Zhang. Small cluster underwater robot design with variable pitch propeller. In *2018 15th International Conference on Ubiquitous Robots (UR)*, pages 235–240. IEEE, 2018.

[22] Abdalati Alhaj, Gerry Vincent Geyer, and Steven Liu. Optimized hardware implementation of foc for bldcs in uavs using a 2-dof pi (blended pi-ip) controller and pso. In *2025 2nd International Conference on Advanced Innovations in Smart Cities (ICAISC)*, pages 1–6. IEEE, 2025.

[23] Dongil Choi. Development of open-source motor controller framework for robotic applications. *IEEE Access*, 8:14134–14145, 2020.

[24] Daniel Mellinger and Vijay Kumar. Minimum snap trajectory generation and control for quadrotors. In *2011 IEEE international conference on robotics and automation*, pages 2520–2525. IEEE, 2011.

[25] Matthias Faessler, Antonio Franchi, and Davide Scaramuzza. Differential flatness of quadrotor dynamics subject to rotor drag for accurate tracking of high-speed trajectories. *IEEE Robotics and Automation Letters*, 3(2):620–626, 2017.

[26] Michael Watterson and Vijay Kumar. Control of quadrotors using the hopf fibration on  $SO(3)$ . In *Robotics Research: The 18th International Symposium ISRR*, pages 199–215. Springer, 2019.

[27] Zhepei Wang, Chao Xu, and Fei Gao. Robust trajectory planning for spatial-temporal multi-drone coordination in large scenes. In *2022 IEEE/RSJ International Conference on Intelligent Robots and Systems (IROS)*, pages 12182–12188. IEEE, 2022.

[28] Zhepei Wang, Xin Zhou, Chao Xu, and Fei Gao. Geometrically constrained trajectory optimization for multicopters. *IEEE Transactions on Robotics*, 38(5):3259–3278, 2022.

[29] Texas Instruments Europe. *Field Orientated Control of 3-Phase AC Motors*, September 1998. Literature Number BPRA073.

[30] Boris Houska, Hans Joachim Ferreau, and Moritz Diehl. Acado toolkit—an open-source framework for automatic control and dynamic optimization. *Optimal control applications and methods*, 32(3):298–312, 2011.

[31] Hans Joachim Ferreau, Christian Kirches, Andreas Potschka, Hans Georg Bock, and Moritz Diehl. qposse: A parametric active-set algorithm for quadratic programming. *Mathematical Programming Computation*, 6(4):327–363, 2014.

[32] Yufan Liu, Cheng Li, Junjie Li, Zemin Lin, Wei Meng, and Fumin Zhang. Wukong: Design, modeling and control of a compact flexible hybrid aerial-aquatic vehicle. *IEEE Robotics and Automation Letters*, 2024.



**Xiangyu Li** received the B.S. degree in electronic information engineering from China Jiliang University, Hangzhou, China, in 2023. He is currently pursuing the M.S. degree in Electronic Information at Zhejiang University, Hangzhou, China. His research interests include multi-domain robot design and control.



**Mingwei Lai** received the B.S. degree in Automation from Huazhong University of Science and Technology in 2023. He is currently working toward the M.S. degree in Control Science and Engineering from Zhejiang University. His research interests include motion planning and MPC control.



**Mengke Zhang** received the B.Eng. degree in Automation from Zhejiang University, Hangzhou, China, in 2021. He is currently pursuing the Ph.D. degree at the Fast Lab, Zhejiang University. His research interests include motion planning and uneven terrains.



**Junxiao Lin** (Student Member, IEEE) received the B.Eng. degree in mechanical engineering from Zhejiang University, Hangzhou, China, in 2023, where he is currently pursuing the M.Phil. degree in control engineering. His research interests include mobile robots, design and control.



**Tiancheng Lai** received the B.S. degree in automation and engineering from the Harbin Institute of Technology, Shenzhen, China, in 2024. He is currently pursuing the M.S. degree in control science and engineering in the Fast Lab at Zhejiang University, Zhejiang, China. His current research interests include motion planning and autonomous exploration of unmanned systems and aerial robots.



**Junping Zhi** graduated from Hainan University in 2009 with a Bachelor's degree in Mechanical Design, Manufacturing, and Automation. He is currently engaged in the maintenance and management of automated tobacco machinery. In addition, he is conducting collaborative research with the Zhejiang University Huzhou Institute, focusing on visual imaging technology and the application of unmanned aerial vehicles within the tobacco processing sector.



**Chao Xu** received the Ph.D. degree in mechanical engineering from Lehigh University in 2010. He is currently the Associate Dean and a Professor with the College of Control Science and Engineering, Zhejiang University. He is the Inaugural Dean of ZJU Huzhou Institute. His research expertise is flying robotics and control-theoretic learning. He has published over 100 articles in international journals, including *Science Robotics* and *Nature Machine Intelligence*. He was the organization committee of the IROS-2025 in Hangzhou.



**Fei Gao** received the Ph.D. degree in electronic and computer engineering from the Hong Kong University of Science and Technology, Hong Kong, in 2019. He is currently a tenured associate professor at the Department of Control Science and Engineering, Zhejiang University. His research interests include aerial robots, autonomous navigation, motion planning, optimization, and localization and mapping.



**Yanjun Cao** received his Ph.D. degree in computer and software engineering from the University of Montreal, Polytechnique Montreal, Canada, in 2020. He is currently an associate researcher at the Huzhou Institute of Zhejiang University, as a PI in the Center of Swarm Navigation. He leads the Field Intelligent Robotics Engineering group of the Field Autonomous System and Computing Lab. His research focuses on key challenges in multi-robot systems, such as collaborative localization, autonomous navigation, perception and communication.